

# Months-long crustal deformation driven by aseismic slips and pore pressure transients triggered by local and regional earthquakes

Zhou Lu<sup>1</sup> and Lianxing Wen<sup>2</sup>

<sup>1</sup>University of Science and Technology of China

<sup>2</sup>State University of New York at Stony Brook

November 24, 2022

## Abstract

Strong strain and pore pressure changes are observed after three Mw 4.5+ local and one Mw 7.2 regional earthquakes during 2010-2017 in borehole strainmeters near Anza, California. The strain change emerges immediately after the earthquakes and lasts 40-100 days with amplitudes up to  $1e-7$ , larger than the coseismic strain offsets. The pore pressure exhibits change immediately after the earthquakes at some boreholes and with a delay of 4-10 days at the others. A joint analysis of the observed postseismic strain and pore pressure change suggests that the postseismic strains could be explained by combined effects of poroelastic deformation due to earthquake-induced pore pressure change and elastic deformation due to an earthquake-triggered aseismic slip on a nearby fault. Our study indicates that, in addition to possible aseismic fault slips triggered by an earthquake, pore pressure changes after the earthquake could be even more important in producing postseismic deformation.

1     **Months-long crustal deformation driven by aseismic slips**  
2     **and pore pressure transients triggered by local and regional**  
3                     **earthquakes**

4  
5                     **Zhou Lu<sup>1\*</sup>, Lianxing Wen<sup>2</sup>**

6  
7     <sup>1</sup>Laboratory of Seismology and Physics of Earth's Interior; School of Earth and Space  
8     Sciences, University of Science and Technology of China, Hefei, China

9     <sup>2</sup>Department of Geosciences, State University of New York at Stony Brook, Stony  
10    Brook, NY, USA

11  
12    \*Corresponding author: Zhou Lu ([luzhou@mail.ustc.edu.cn](mailto:luzhou@mail.ustc.edu.cn))

13  
14    **Key points:**

- 15    • We observe strong months-long change of strain and pore pressure after four Mw  
16    4.5+ earthquakes in borehole strainmeters at Anza, California
- 17    • The postseismic strains last 40–100 days, and exhibit different trends and larger  
18    amplitudes (up to  $1e^{-7}$ ) compared to coseismic strains
- 19    • Postseismic strains = poroelastic strain by earthquake-induced pore pressure  
20    change + elastic strain by an earthquake-triggered aseismic slip

21

22 **Abstract**

23 Strong strain and pore pressure changes are observed after three Mw 4.5+ local and one  
24 Mw 7.2 regional earthquakes during 2010–2017 in borehole strainmeters near Anza,  
25 California. The strain change emerges immediately after the earthquakes and lasts 40–  
26 100 days with amplitudes up to  $10^{-7}$ , larger than the coseismic strain offsets. The pore  
27 pressure exhibits change immediately after the earthquakes at some boreholes and with  
28 a delay of 4–10 days at the others. A joint analysis of the observed postseismic strain  
29 and pore pressure change suggests that the postseismic strains could be explained by  
30 combined effects of poroelastic deformation due to earthquake-induced pore pressure  
31 change and elastic deformation due to an earthquake-triggered aseismic slip on a nearby  
32 fault. Our study indicates that, in addition to possible aseismic fault slips triggered by  
33 an earthquake, pore pressure changes after the earthquake could be even more important  
34 in producing postseismic deformation.

35

36

## 37 **Plain language summary**

38 Understanding the physical mechanisms producing postseismic deformation is  
39 important for assessing fault slip budget and seismic hazards. In this study, we seek to  
40 clarify possible roles of aseismic slip and pore pressure change in producing  
41 postseismic deformation through a joint analysis of postseismic strains and pore  
42 pressure change observed following four Mw 4.5+ earthquakes in southern California.  
43 The postseismic strains start immediately after the earthquakes and last 40–100 days.  
44 They also exhibit larger amplitudes and different relative amplitudes among different  
45 strain components compared to the coseismic strain offsets. The pore pressure exhibits  
46 postseismic changes immediately after the earthquakes in some boreholes and with a  
47 delay of 4–10 days at the others. These observations are well explained by a mechanism  
48 that the mainshock earthquake instantly triggers an aseismic slip in a neighboring fault  
49 and alters the hydrological conditions in the region; the change of hydrological  
50 condition results in postseismic pore pressure changes and produces poroelastic  
51 deformation in the region, while the aseismic slip produces elastic deformation. This  
52 study indicates that, in addition to possible aseismic fault slips triggered by an  
53 earthquake, pore pressure changes after the earthquake could play an even more  
54 important role in producing postseismic deformation.

55

56

## 57 **1. Introduction**

58 Understanding postseismic deformation is important for assessing seismic hazards as  
59 the deformation changes fault slip budget and stress state in seismogenic zones  
60 (Gualandi et al., 2020; Iinuma et al., 2016; Johanson et al., 2006; Xu et al., 2020).

61 Postseismic deformation can be induced by many physical mechanisms and is useful  
62 for constraining many physical properties of the Earth. For example, postseismic  
63 deformation induced by an aseismic slip is useful for constraining fault frictional  
64 properties (Johnson et al., 2006), while that related to viscoelastic relaxation of the  
65 coseismic deformation is routinely used to infer rheological properties of the lower  
66 crust and upper mantle (Hu et al., 2016; Jónsson, 2008; Nur & Mavko, 1974).

67 Additionally, postseismic deformation produced by pore fluid flow can also be used to  
68 constrain near surface hydrological properties (Jónsson et al., 2003; Peltzer et al., 1998).

69

70 Postseismic deformation produced by aseismic slip has attracted close attentions from  
71 various studies. For example, such deformation has been observed in the nature by  
72 many instruments, including theodolite (Scholz et al., 1969; Smith & Wyss, 1968), GPS  
73 (Johnson et al., 2006; Yu et al., 2003), InSAR (Johanson et al., 2006), strainmeter  
74 (Alwahedi & Hawthorne, 2019; Hawthorne et al., 2016; Inbal et al., 2017), and sea  
75 floor geodetic observation (Iinuma et al., 2016). Additionally, postseismic aseismic slip  
76 has also been generated in numerical simulations (Helmstetter & Shaw, 2009).

77

78 By contrast, postseismic deformation produced by pore fluid has been reported by only

79 a few studies (e.g., Hughes et al., 2010; Jónsson et al., 2003; Peltzer et al., 1998).  
80 However, such fluid-related postseismic deformation is likely significant in the crust,  
81 as some earthquakes have been reported to induce significant changes in hydrological  
82 conditions (Manga & Wang, 2007; Matsumoto et al., 2003; Roeloffs, 1998; C.-Y. Wang  
83 et al., 2004) and crustal deformation related to hydrological process has been observed  
84 to be significant (Fu & Freymueller, 2012; Lu & Wen, 2018; Silverii et al., 2019; C.-Y.  
85 Wang & Barbour, 2017; Zhan et al., 2017).

86  
87 Distinguishing between postseismic pore fluid and aseismic slip from field observations  
88 and understanding the role of each mechanism in producing postseismic deformation  
89 are critical for inferring the related geophysical processes and properties of the Earth,  
90 as these two processes have been reported to be closely related after some earthquakes.  
91 For example, both theoretical analysis and numerical modeling have shown that pore  
92 fluid flow after an earthquake plays an important role in fault slip (Byerlee, 1993;  
93 Sibson, 1992), and fluid pressure change following the 2016 Kaikōura, New Zealand  
94 earthquake has also been inferred to drive aseismic fault slip (Hamling & Upton, 2018).  
95 So far, many previous studies have considered separately the roles of postseismic pore  
96 fluid and aseismic slip in explaining postseismic deformations (e.g., Alwahedi &  
97 Hawthorne, 2019; Inbal et al., 2017; Jónsson et al., 2003; Peltzer et al., 1998) or have  
98 combined the two processes for only large earthquakes (c.f.,  $M_w > 6$ ) (Kang Wang &  
99 Fialko, 2018). Few studies combine these two processes to explore their interplay in  
100 explaining some of the postseismic deformations, although these two processes have

101 been reported to be closely related as discussed above.

102

103 In this study, we seek to clarify possible roles of aseismic slip and pore pressure change  
104 in producing postseismic deformation through a joint analysis of postseismic strains  
105 and pore pressure change observed following four Mw 4.5+ earthquakes in southern  
106 California. We report the observation of strong postseismic changes of strain and pore  
107 pressure in section 2, and discuss possible physical mechanisms in section 3.

108

## 109 **2. Observation of strong postseismic changes of strain and** 110 **pore pressure**

111 We use the strain data recorded in the Network of the Americas (NOTA) borehole  
112 strainmeters and the pore pressure data recorded in the strainmeter boreholes to study  
113 postseismic deformation (Figure 1a). The NOTA strainmeters are placed in boreholes  
114 at depths of 120–250 m along the plate boundary zones of the western United States  
115 and on Vancouver Island of Canada (Silver & PBO Steering Committee, 2000). Each  
116 strainmeter consists of four horizontal gauges that measure elongation of the  
117 surrounding rock at different directions with a resolution of about  $10^{-10}$  (Gladwin, 1984).  
118 Those gauge measurements could be converted into a horizontal strain tensor through  
119 calibration matrixes obtained based on tidal response (Hodgkinson et al., 2013;  
120 Roeloffs, 2010). Auxiliary data are also measured at the strainmeter sites, including  
121 barometric pressure and rainfall at all sites, and pore pressure at some sites in Cascadia

122 and California. Since installation in 2005, strain signals are observed in the strainmeters  
123 related to many geophysical phenomena, including tide (Hodgkinson et al., 2013; Lu &  
124 Wen, 2017; Roeloffs, 2010), earthquake (Barbour et al., 2014; Inbal et al., 2017;  
125 Roeloffs, 2010), postseismic slip (Alwahedi & Hawthorne, 2019; Hawthorne et al.,  
126 2016; Inbal et al., 2017), aseismic creep (Langbein, 2010; Roeloffs, 2010), episodic  
127 tremor and slip (Dragert & Wang, 2011; Hawthorne & Rubin, 2010; Kelin Wang et al.,  
128 2008), hydrological deformation (Barbour, 2015; Barbour & Wyatt, 2014; Lu & Wen,  
129 2018), and lake seiche (Luttrell et al., 2013).

130

131 We download the NOTA borehole strain (level 2) and pore pressure data from  
132 UNAVCO. We eliminate data outliers, remove barometric pressure response, tidal  
133 signal and borehole trend from the original strain data, and obtain the residual strain  
134 signal. We further use the tidal calibration matrixes (Hodgkinson et al., 2013) to convert  
135 the residual strain from four-gauge measurements to horizontal strain tensor  
136 components, including areal strain  $E_A = \varepsilon_{ee} + \varepsilon_{nn}$ , differential extension  $E_D = \varepsilon_{ee} -$   
137  $\varepsilon_{nn}$  and engineering shear strain  $E_S = 2\varepsilon_{en}$ , where  $\varepsilon_{ee}$  and  $\varepsilon_{nn}$  are east-west and  
138 north-south normal strains, respectively, and  $\varepsilon_{en}$  is east-north shear strain.

139

140 Strong postseismic deformation signals (with an amplitude up to  $10^{-7}$ ) are observed in  
141 the residual strain data recorded near Anza, southern California. These signals start  
142 immediately after three local earthquakes ( $M_w > 4.5$ ) and one remote earthquake ( $M_w$   
143 7.2), and last 40–100 days (Figures 1–2 and S1–S2). The postseismic strains of the four

144 earthquakes exhibit similar behaviors, with the postseismic strain at a same gauge of a  
145 strainmeter either consistently increasing or decreasing for all the four earthquakes  
146 (Figures 2 and S1–S2). The strain rate is large immediately after the earthquakes and  
147 decreases over time, with the decreasing rate varying significantly among different  
148 strainmeters (Figure 2). Compared to the coseismic static strains, the postseismic strains  
149 exhibit larger amplitudes and different relative amplitudes among different strain  
150 components (Figure 2).

151

152 The pore pressure recorded at some of the strainmeters also exhibits significant  
153 postseismic changes ( $10^3$ – $10^4$  Pa), with the observations of the four earthquakes  
154 exhibiting similar increasing or decreasing trend at a same strainmeter (Figures 1–2 and  
155 S1–S2). However, the postseismic pore pressure exhibits different behaviors among  
156 different strainmeters (Figure 2). At some strainmeters, pore pressure decreases  
157 immediately after the earthquakes. For example, pore pressure at B087 decreases  
158 immediately after the 2016 Mw 5.2 earthquake, concurrent with the postseismic strain  
159 (Figure 2c). At some other strainmeters, the pore pressure decrease has a time delay of  
160 4–10 days relative to the occurrence of the earthquakes. For example, pore pressure  
161 remains at background level at B086 for about 8 days after the 2016 Mw 5.2 earthquake  
162 before exhibiting a significant decrease (Figures 2b and S3). At the other strainmeters,  
163 pore pressure exhibits only small or no postseismic changes (Figures 2e and 2f).

164

### 165 **3. Physical mechanisms for the postseismic strains**

166 As the four earthquakes exhibit similar postseismic behaviors and the data quality for  
167 the 2016 Mw 5.2 earthquake is the best among the four earthquakes (Figure 2), we use  
168 the observations of this earthquake as an example to explore physical mechanisms for  
169 the postseismic strains.

170

171 The observed strong postseismic strains cannot be explained by postseismic  
172 viscoelastic relaxation, as the relaxation usually produces postseismic strain smaller in  
173 amplitude compared to the coseismic static strain on the timescale of several to tens of  
174 days, contrary to the observations (Figure 2). Nor can these observed postseismic  
175 strains be explained by the fault slip produced by the aftershocks, because the total  
176 coseismic static strains produced by the aftershocks are at orders of  $10^{-11}$ – $10^{-10}$  (Figure  
177 S4), about 3 orders of magnitude smaller than the observed postseismic strains. Besides,  
178 the strains produced by the aftershocks would exhibit different temporal variations from  
179 those observed in the postseismic strains (Figure S4).

180

181 The correlation between the observed postseismic strains and the postseismic pore  
182 pressure changes suggests that at least some of the postseismic strains are likely  
183 hydrological in origin. However, the postseismic strains cannot purely be caused by the  
184 postseismic pore pressure changes based on the postseismic observations from  
185 strainmeters B086 and B084. Note that the strains start changing immediately after the  
186 2016 Mw 5.2 earthquake at B086, but the pore pressure only starts significantly

187 decreasing with a delay of 8 days (Figures 2b and S3). At B084, the pore pressure  
188 change after the 2016 Mw 5.2 earthquake lasts only about 10 days, while the  
189 postseismic strain lasts at least 30 days (Figure 2a). These postseismic strains observed  
190 immediately after the earthquake without concurrent pore pressure changes suggest that  
191 the observed postseismic strains cannot purely be explained by the postseismic pore  
192 pressure changes alone, and there should be an additional mechanism that produces the  
193 observed postseismic strains.

194

195 We show that the observed strong postseismic strains could be explained by combined  
196 effects of the postseismic pore pressure change and an earthquake-triggered aseismic  
197 slip on a neighboring fault to the mainshock. We decompose the observed postseismic  
198 strains into two parts, with one part related to the pore pressure change and the other  
199 part produced by an aseismic slip:

$$200 \quad d_{ij}(t) = f_{ij}P_j(t) + G_{ij}M(t), \quad (1)$$

201 where  $t$  is time,  $d_{ij}$  postseismic strain observed at the  $i$ th component ( $E_A$ ,  $E_D$  or  
202  $E_S$ ) of the  $j$ th strainmeter,  $P_j$  observed postseismic pore pressure change,  $f_{ij}$   
203 proportional factor of the pressure-induced strain to the pore pressure change,  $M$   
204 seismic moment of the aseismic slip, and  $G_{ij}$  Green's function of static strain produced  
205 by a unit aseismic slip. On the right hand side (RHS) of Equation (1), the first term  
206 represents the strain produced by the pore pressure change, with each component of the  
207 pressure-induced strain at each strainmeter assumed to be linearly proportional to the  
208 postseismic pore pressure change at that strainmeter. The second term represents the

209 strain produced by the aseismic slip, which is assumed to only occur at a point on the  
210 fault plane with a consistent focal mechanism during the aseismic slip period. In  
211 Equation (1),  $d_{ij}(t)$  and  $P_j(t)$  are the observed data, while the other parameters are  
212 unknowns that are inverted from the data.

213

214 We select  $d_{ij}(t)$  and  $P_j(t)$  that are used in Equation (1) based on the data quality of  
215 each strainmeter. We use the data from B084, B086, B087 and B088 for quantitative  
216 constraint of the aseismic slip and pore pressure effect based on Equation (1), as these  
217 strainmeters record clear postseismic signals that exhibit a high signal-to-noise ratio.  
218 For the other strainmeters that exhibit a lower signal-to-noise ratio (B081, B089, B093  
219 and B946), we only use the data from them as qualitative constraints, i.e., we require  
220 that the synthetic postseismic strains produced by the aseismic slip be within the  
221 magnitudes of the strain variations observed at these strainmeters. We only use the data  
222 recorded in the early 30 days after the earthquake, as the cumulative effects of the  
223 background strain variations after 30 days would no longer be small enough to be  
224 ignored in the postseismic strain data.

225

226 We search all possible aseismic slip point sources along the San Jacinto fault zone with  
227 a focal mechanism consistent with the local fault slip, and find a best-fitting solution of  
228  $G_{ij}$ ,  $M(t)$  and  $f_{ij}$  to Equation (1) through minimizing the following error function:

$$229 \quad E = \|f_{ij}P_j(t) + G_{ij}M(t) - d_{ij}(t)\|^2 + \alpha^2 \|LM(t)\|^2, \quad (2)$$

230 where  $\|\cdot\|$  denotes the  $L_2$  norm. On the RHS, the first term is the misfit between the

231 synthetic and observed postseismic strains. This term is a summation of the misfits for  
232 all strain components ( $E_A$ ,  $E_D$  and  $E_S$ ) of the strainmeters selected as quantitative  
233 constraints (B084, B086, B087 and B088) through 0–30 days after the earthquake.  $G_{ij}$   
234 is computed using an elastic half-space Earth model (Okada, 1985) with elastic moduli  
235  $\lambda = 37.2$  GPa and  $\mu = 36.8$  GPa (Laske et al., 2013). The second term is a  
236 regularization term that imposes a temporal smoothness on the aseismic fault slip, with  
237  $L$  being the second-order Tikhonov regularization operator and  $\alpha$  being a smoothness  
238 coefficient that controls the relative importance between the misfit and smoothness  
239 terms. The value of  $\alpha$  is determined through an L-curve analysis, being  $4 \times$   
240  $10^{-29}$  day<sup>2</sup>/dyne · cm (Figure S5).

241

242 The best-fitting aseismic solution corresponds to an aseismic slip at depth of 5 km and  
243 located 11 km north and 6 km west to the 2016 Mw 5.2 earthquake, with an equivalent  
244 magnitude of Mw 4.9 accumulated in the early 30-day's postseismic period and a focal  
245 mechanism of strike/dip/rake = 283°/83°/199° (Figures 3a and 3b). The moment rate of  
246 the aseismic slip decreases logarithmically over time after the mainshock and has not  
247 reached zero at the 30<sup>th</sup> postseismic day (Figure 3a). The absolute value of the best-  
248 fitting strain-pressure proportional factor ranges between  $2-125 \times 10^{-10}$ /Pa for different  
249 strain components of the strainmeters. Overall, the total strains of the inferred solutions  
250 of aseismic slip and pore pressure-induced deformation fit the observed strains well for  
251 those selected for the quantitative inversion (Figure 3). The principal strains of the  
252 synthetic strains accumulated in the early 20-day's postseismic period are consistent

253 with those of the observed residual strains in both orientation and amplitude (Figure  
254 3b). With the exceptions for the components that contain noise unrelated to the  
255 postseismic deformation (c.f., the sudden strain change of  $E_S$  at B088 in the second  
256 postseismic day), the synthetic time series of the postseismic strains match the observed  
257 time series well (Figures 3c–3e). At B086, the strains observed in the early 8-day's  
258 postseismic period are mainly explained by the aseismic slip, as the pore pressure  
259 change is small in this time period. Additionally, the synthetic postseismic strains  
260 produced by the inferred aseismic slip are also within the magnitudes of the strain  
261 variations observed at the other strainmeters that are not used as the quantitative  
262 constraints (Figure S6).

263

264 Based on the above modeling results, we propose a mechanism that the mainshock  
265 event instantly triggers an aseismic slip in a neighboring fault and alters the  
266 hydrological conditions in the region; the change of hydrological condition results in  
267 postseismic pore pressure changes and produces poroelastic deformation in the region,  
268 while the aseismic slip produces elastic deformation (Figure 4). Such mechanism is  
269 consistent with the results of our previous study on hydro-related strain at Anza which  
270 shows that underground pore fluid could produce significant poroelastic deformation  
271 (Lu & Wen, 2018). For the current earthquakes, additional supporting evidence includes:  
272 (1) Observation of the postseismic pore pressure change at the multiple strainmeters  
273 suggests a broad distribution of pore pressure change, which could produce poroelastic  
274 deformation in a broad region, (2) the significant differences of the postseismic pore

275 pressure change observed among the strainmeters suggest a significant spatial variation  
276 of the pore pressure change, which would further promote the poroelastic deformation,  
277 and (3) the persistent pore pressure changes observed after all the four earthquakes  
278 suggest that the pore fluid would likely change after every large earthquake at the region  
279 and produce persistent poroelastic deformation.

280

281 We have made two simplifications in the modeling of the observed postseismic strains.  
282 First, we have adopted a point source for the aseismic slip model, while a realistic  
283 aseismic slip would likely occur with a finite spatial distribution on the fault plane. In  
284 the absence of dense geodetic observations in the region, our choice of the point source  
285 model for the aseismic slip is a balance between explaining the observed strain data and  
286 avoiding overfitting the limited data set. Despite the point source simplification, the  
287 existence of the aseismic slip and the decomposition of the slip-related strain from the  
288 hydro-related strain are well resolved by the observed residual strain and pore pressure  
289 data. Second, we have assumed that the strain induced by the pore pressure change is  
290 proportional to the pore pressure change recorded at the site, while the strain should be  
291 related to the spatial and temporal changes of pore pressure in the region. While the  
292 lack of detailed 3D observations of pore pressure renders the detailed poroelastic  
293 modeling impossible, the inferred quantitative relationships between the pore pressure  
294 change and the residual strain should be interpreted with caution. However, we believe  
295 the linear relationship between the pressure-induced strain and the postseismic pore  
296 pressure change is a good assumption based on the high correlation of the time series

297 between the two observations and the fact that they are recorded at the same sites.

298

## 299 **4. Conclusions**

300 Strong months-long changes of strain and pore pressure are observed after three Mw  
301 4.5+ local and one Mw 7.2 regional earthquakes during 2010–2017 in the NOTA  
302 borehole strainmeters near Anza, southern California. The strain change emerges  
303 immediately after the earthquakes and last 40–100 days. The postseismic strains of the  
304 four earthquakes exhibit similar behaviors, with the postseismic strain at a same gauge  
305 of a strainmeter either consistently increasing or decreasing for all the four earthquakes.  
306 Compared to the coseismic strain offsets, the postseismic strains exhibit larger  
307 amplitudes (up to  $10^{-7}$ ) and different relative amplitudes among different strain  
308 components. The postseismic pore pressure exhibits similar increasing or decreasing  
309 trend ( $10^3$ – $10^4$  Pa) for the four earthquakes at a same strainmeter, but exhibits different  
310 behaviors among different strainmeters, with changing immediately after the  
311 earthquakes at some sites and exhibiting a time delay of 4–10 days relative to the  
312 occurrence of the earthquakes at the others. The observed postseismic strains can be  
313 explained by combined effects of poroelastic deformation due to the pore pressure  
314 change and elastic deformation due to an aseismic slip on a neighboring fault. Based  
315 on the modeling results, we propose a mechanism that the mainshock event instantly  
316 triggers an aseismic slip in a neighboring fault and alters the hydrological conditions in  
317 the region; the change of hydrological condition results in postseismic pore pressure

318 changes and produces poroelastic deformation in the region, while the aseismic slip  
319 produces elastic deformation Our study indicates that, in addition to possible aseismic  
320 fault slips triggered by an earthquake, pore pressure changes after the earthquake could  
321 play an even more important role in producing postseismic deformation.

322

323

324

## 325 **Acknowledgements**

326 The NOTA borehole strain and pore pressure data were downloaded from UNAVCO  
327 (<http://www.unavco.org/data/strain-seismic/strain-seismic.html/>). The figures in the  
328 article were prepared using GMT package (Wessel et al., 2013) and Power Point. This  
329 research was supported by the China Postdoctoral Science Foundation under grant  
330 2019TQ0301; the National Natural Science Foundation of China under grants  
331 41874002 and 41674045; the Key Research Program of Frontier Sciences of Chinese  
332 Academy of Sciences (QYZDY-SSW-DQC020, CAS); and the Natural Science  
333 Foundation of Anhui Province of China.

334

335

336 **References**

- 337 Alwahedi, M. A., & Hawthorne, J. C. (2019). Intermediate-magnitude postseismic slip  
338 follows intermediate-magnitude ( $M$  4 to 5) earthquakes in California.  
339 *Geophysical Research Letters*, 46(7), 3676–3687. doi:10.1029/2018gl081001
- 340 Barbour, A. J. (2015). Pore pressure sensitivities to dynamic strains: Observations in  
341 active tectonic regions. *Journal of Geophysical Research: Solid Earth*, 120(8),  
342 5863–5883. doi:10.1002/2015JB012201
- 343 Barbour, A. J., Agnew, D. C., & Wyatt, F. K. (2014). Coseismic strains on Plate  
344 Boundary Observatory borehole strainmeters in Southern California. *Bulletin of*  
345 *the Seismological Society of America*, 105(1), 431–444. doi:10.1785/0120140199
- 346 Barbour, A. J., & Wyatt, F. K. (2014). Modeling strain and pore pressure associated  
347 with fluid extraction: The Pathfinder Ranch experiment. *Journal of Geophysical*  
348 *Research: Solid Earth*, 119(6), 5254–5273. doi:10.1002/2014JB011169
- 349 Byerlee, J. (1993). Model for episodic flow of high-pressure water in fault zones before  
350 earthquakes. *Geology*, 21(4), 303–306. doi:10.1130/0091-  
351 7613(1993)021<0303:mfeoh>2.3.co;2
- 352 Dragert, H., & Wang, K. (2011). Temporal evolution of an episodic tremor and slip  
353 event along the northern Cascadia margin. *Journal of Geophysical Research*,  
354 116(B12), B12406. doi:10.1029/2011JB008609
- 355 Fu, Y., & Freymueller, J. T. (2012). Seasonal and long-term vertical deformation in the  
356 Nepal Himalaya constrained by GPS and GRACE measurements. *Journal of*  
357 *Geophysical Research*, 117(B3), B03407. doi:10.1029/2011JB008925

358 Gladwin, M. T. (1984). High-precision multicomponent borehole deformation  
359 monitoring. *Review of Scientific Instruments*, 55(12), 2011–2016.  
360 doi:10.1063/1.1137704

361 Gualandi, A., Liu, Z., & Rollins, C. (2020). Post-large earthquake seismic activities  
362 mediated by aseismic deformation processes. *Earth and Planetary Science  
363 Letters*, 530, 115870. doi:10.1016/j.epsl.2019.115870

364 Hamling, I. J., & Upton, P. (2018). Observations of aseismic slip driven by fluid  
365 pressure following the 2016 Kaikōura, New Zealand, earthquake. *Geophysical  
366 Research Letters*, 45(20), 11030–11039. doi:10.1029/2018GL079224

367 Hawthorne, J. C., & Rubin, A. M. (2010). Tidal modulation of slow slip in Cascadia.  
368 *Journal of Geophysical Research*, 115(B9), B09406. doi:10.1029/2010jb007502

369 Hawthorne, J. C., Simons, M., & Ampuero, J. P. (2016). Estimates of aseismic slip  
370 associated with small earthquakes near San Juan Bautista, CA. *Journal of  
371 Geophysical Research: Solid Earth*, 121(11), 8254–8275.  
372 doi:10.1002/2016jb013120

373 Helmstetter, A., & Shaw, B. E. (2009). Afterslip and aftershocks in the rate-and-state  
374 friction law. *Journal of Geophysical Research*, 114(B1), B01308.  
375 doi:10.1029/2007jb005077

376 Hodgkinson, K., Langbein, J., Henderson, B., Mencin, D., & Borsa, A. (2013). Tidal  
377 calibration of plate boundary observatory borehole strainmeters. *Journal of  
378 Geophysical Research: Solid Earth*, 118(1), 447–458.  
379 doi:10.1029/2012JB009651

380 Hu, Y., Bürgmann, R., Banerjee, P., Feng, L., Hill, E. M., Ito, T., . . . Wang, K. (2016).  
381 Asthenosphere rheology inferred from observations of the 2012 Indian Ocean  
382 earthquake. *Nature*, 538(7625), 368–372. doi:10.1038/nature19787

383 Hughes, K. L. H., Masterlark, T., & Mooney, W. D. (2010). Poroelastic stress-triggering  
384 of the 2005 M8.7 Nias earthquake by the 2004 M9.2 Sumatra–Andaman  
385 earthquake. *Earth and Planetary Science Letters*, 293(3–4), 289–299.  
386 doi:10.1016/j.epsl.2010.02.043

387 Inuma, T., Hino, R., Uchida, N., Nakamura, W., Kido, M., Osada, Y., & Miura, S.  
388 (2016). Seafloor observations indicate spatial separation of coseismic and  
389 postseismic slips in the 2011 Tohoku earthquake. *Nature Communications*, 7,  
390 13506. doi:10.1038/ncomms13506

391 Inbal, A., Ampuero, J.-P., & Avouac, J.-P. (2017). Locally and remotely triggered  
392 aseismic slip on the central San Jacinto Fault near Anza, CA, from joint inversion  
393 of seismicity and strainmeter data. *Journal of Geophysical Research: Solid Earth*,  
394 122(4), 3033–3061. doi:10.1002/2016jb013499

395 Johanson, I. A., Fielding, E. J., Rolandone, F., & Bürgmann, R. (2006). Coseismic and  
396 postseismic slip of the 2004 Parkfield earthquake from space-geodetic data.  
397 *Bulletin of the Seismological Society of America*, 96(4B), S269–S282.  
398 doi:10.1785/0120050818

399 Johnson, K. M., Johnson, K. M., Bürgmann, R., & Larson, K. (2006). Frictional  
400 properties on the San Andreas fault near Parkfield, California, inferred from  
401 models of afterslip following the 2004 earthquake. *Bulletin of the Seismological*

402           *Society of America*, 96(4B), S321–S338. doi:10.1785/0120050808

403   Jónsson, S. (2008). Importance of post-seismic viscous relaxation in southern Iceland.

404           *Nature Geoscience*, 1(2), 136–139. doi:10.1038/ngeo105

405   Jónsson, S., Segall, P., Pedersen, R., & Björnsson, G. (2003). Post-earthquake ground

406           movements correlated to pore-pressure transients. *Nature*, 424(6945), 179–183.

407           doi:10.1038/nature01776

408   Langbein, J. (2010). Effect of error in theoretical Earth tide on calibration of borehole

409           strainmeters. *Geophysical Research Letters*, 37(21), L21303.

410           doi:10.1029/2010GL044454

411   Laske, G., Masters., G., Ma, Z., & Pasyanos, M. (2013). *Update on CRUST1.0 - A 1-*

412           *degree global model of Earth's crust*. Paper presented at the EGU.

413   Lu, Z., & Wen, L. (2017). Abnormally strong daily-cycle S<sub>1</sub> strain tide: Observation

414           and physical mechanism. *Journal of Geophysical Research: Solid Earth*, 122(10),

415           8525–8537. doi:10.1002/2017JB014383

416   Lu, Z., & Wen, L. (2018). Strong hydro - related localized long - period crustal

417           deformation observed in the Plate Boundary Observatory borehole strainmeters.

418           *Geophysical Research Letters*, 45(23), 12856 – 12865.

419           doi:10.1029/2018gl080856

420   Luttrell, K., Mencin, D., Francis, O., & Hurwitz, S. (2013). Constraints on the upper

421           crustal magma reservoir beneath Yellowstone Caldera inferred from lake-seiche

422           induced strain observations. *Geophysical Research Letters*, 40(3), 501–506.

423           doi:10.1002/grl.50155

424 Manga, M., & Wang, C.-Y. (2007). Earthquake hydrology. In H. Kanamori & G.  
425 Schubert (Eds.), *Treatise on Geophysics* (Vol. 4, pp. 293–320). Amsterdam:  
426 Elsevier.

427 Matsumoto, N., Kitagawa, G., & Roeloffs, E. A. (2003). Hydrological response to  
428 earthquakes in the Haibara well, central Japan - I. Groundwater level changes  
429 revealed using state space decomposition of atmospheric pressure, rainfall and  
430 tidal responses. *Geophysical Journal International*, 155(3), 885–898.  
431 doi:10.1111/j.1365-246X.2003.02103.x

432 Nur, A., & Mavko, G. (1974). Postseismic viscoelastic rebound. *Science*, 183(4121),  
433 204–206. doi:10.1126/science.183.4121.204

434 Okada, Y. (1985). Surface deformation due to shear and tensile faults in a half-space.  
435 *Bulletin of the Seismological Society of America*, 75(4), 1135–1154.

436 Peltzer, G., Rosen, P., Rogez, F., & Hudnut, K. (1998). Poroelastic rebound along the  
437 Landers 1992 earthquake surface rupture. *Journal of Geophysical Research*,  
438 103(B12), 30131–30145. doi:10.1029/98jb02302

439 Roeloffs, E. A. (1998). Persistent water level changes in a well near Parkfield,  
440 California, due to local and distant earthquakes. *Journal of Geophysical Research*,  
441 103(B1), 869–889. doi:10.1029/97jb02335

442 Roeloffs, E. A. (2010). Tidal calibration of Plate Boundary Observatory borehole  
443 strainmeters: Roles of vertical and shear coupling. *Journal of Geophysical*  
444 *Research*, 115, B06405. doi:10.1029/2009JB006407

445 Ross, Z. E., Kanamori, H., & Hauksson, E. (2017). Anomalously large complete stress

446 drop during the 2016 Mw 5.2 Borrego Springs earthquake inferred by waveform  
447 modeling and near-source aftershock deficit. *Geophysical Research Letters*,  
448 *44*(12), 5994–6001. doi:10.1002/2017gl073338

449 Scholz, C. H., Wyss, M., & Smith, S. W. (1969). Seismic and aseismic slip on the San  
450 Andreas fault. *Journal of Geophysical Research*, *74*(8), 2049–2069.  
451 doi:10.1029/JB074i008p02049

452 Sibson, R. H. (1992). Implications of fault-valve behaviour for rupture nucleation and  
453 recurrence. *Tectonophysics*, *211*(1–4), 283–293. doi:10.1016/0040-  
454 1951(92)90065-e

455 Silver, P. G., & PBO Steering Committee. (2000). The Plate Boundary Observatory  
456 white paper: Creating a four-D image of the deformation of western North  
457 America.

458 Silverii, F., D'Agostino, N., Borsa, A. A., Calcaterra, S., Gambino, P., Giuliani, R., &  
459 Mattone, M. (2019). Transient crustal deformation from karst aquifers hydrology  
460 in the Apennines (Italy). *Earth and Planetary Science Letters*, *506*, 23–37.  
461 doi:10.1016/j.epsl.2018.10.019

462 Smith, S. W., & Wyss, M. (1968). Displacement on the San Andreas fault subsequent  
463 to the 1966 Parkfield earthquake. *Bulletin of the Seismological Society of America*,  
464 *58*(6), 1955–1973.

465 Wang, C.-Y., & Barbour, A. J. (2017). Influence of pore pressure change on coseismic  
466 volumetric strain. *Earth and Planetary Science Letters*, *475*, 152–159.  
467 doi:10.1016/j.epsl.2017.07.034

468 Wang, C.-Y., Wang, C.-H., & Manga, M. (2004). Coseismic release of water from  
469 mountains: Evidence from the 1999 (Mw = 7.5) Chi-Chi, Taiwan, earthquake.  
470 *Geology*, 32(9), 769–772. doi:10.1130/g20753.1

471 Wang, K., Dragert, H., Kao, H., & Roeloffs, E. (2008). Characterizing an  
472 “uncharacteristic” ETS event in northern Cascadia. *Geophysical Research Letters*,  
473 35(15), L15303. doi:10.1029/2008GL034415

474 Wang, K., & Fialko, Y. (2018). Observations and modeling of coseismic and  
475 postseismic deformation due to the 2015 Mw 7.8 Gorkha (Nepal) earthquake.  
476 *Journal of Geophysical Research: Solid Earth*, 123(1), 761–779.  
477 doi:10.1002/2017jb014620

478 Wessel, P., Smith, W. H. F., Scharroo, R., Luis, J., & Wobbe, F. (2013). Generic  
479 Mapping Tools: Improved version released. *Eos, Transactions American*  
480 *Geophysical Union*, 94(45), 409–410. doi:10.1002/2013EO450001

481 Xu, X., Sandwell, D. T., Ward, L. A., Milliner, C. W. D., Smith-Konter, B. R., Fang, P.,  
482 & Bock, Y. (2020). Surface deformation associated with fractures near the 2019  
483 Ridgecrest earthquake sequence. *Science*, 370(6516), 605–608.  
484 doi:10.1126/science.abd1690

485 Yu, S.-B., Hsu, Y.-J., Kuo, L.-C., & Chen, H.-Y. (2003). GPS measurement of  
486 postseismic deformation following the 1999 Chi-Chi, Taiwan, earthquake.  
487 *Journal of Geophysical Research*, 108(B11), 2520. doi:10.1029/2003jb002396

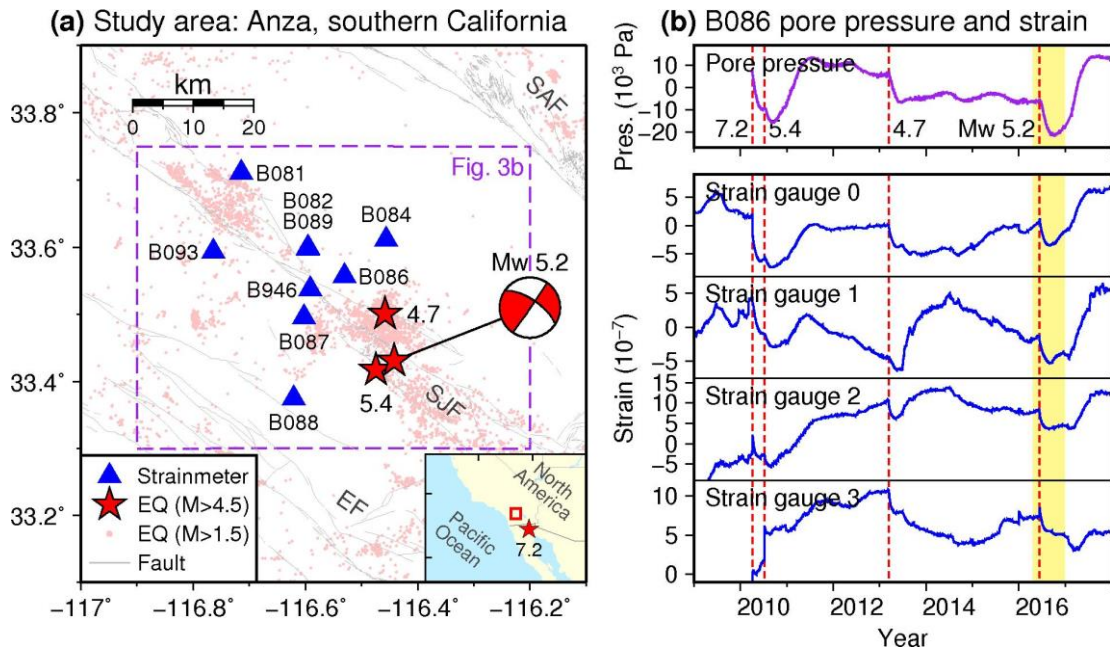
488 Zhan, W., Li, F., Hao, W., & Yan, J. (2017). Regional characteristics and influencing  
489 factors of seasonal vertical crustal motions in Yunnan, China. *Geophysical*

490 *Journal International*, 210(3), 1295–1304. doi:10.1093/gji/ggx246

491

492

493 **Figures and captions**



494

495 **Figure 1. Study area and an example observation of pore pressure and strain from**

496 **strainmeter B086. (a)** Study area showing NOTA strainmeters (blue triangles),

497 earthquakes (red stars and pink points for magnitudes larger than 4.5 and 1.5,

498 respectively) and faults (grey lines) near Anza, southern California, with the strainmeter

499 names, earthquake magnitudes and fault names (SAF: San Andreas fault. SJF: San

500 Jacinto fault. EF: Elsinore fault) labeled. The beach ball represents the focal mechanism

501 (strike/dip/rake =  $304^\circ/68^\circ/179^\circ$ ) of the 10 June 2016 Borrego Springs Mw 5.2

502 earthquake (Ross et al., 2017). The inset shows the map region of Figure 1a within

503 North America (red box) and the location of a regional Mw 7.2 earthquake (red star).

504 **(b)** Pore pressure (purple curve) and strain (blue curves) observed during 2009–2017 at

505 strainmeter B086, with the occurrence time of the four Mw 4.5+ earthquakes marked

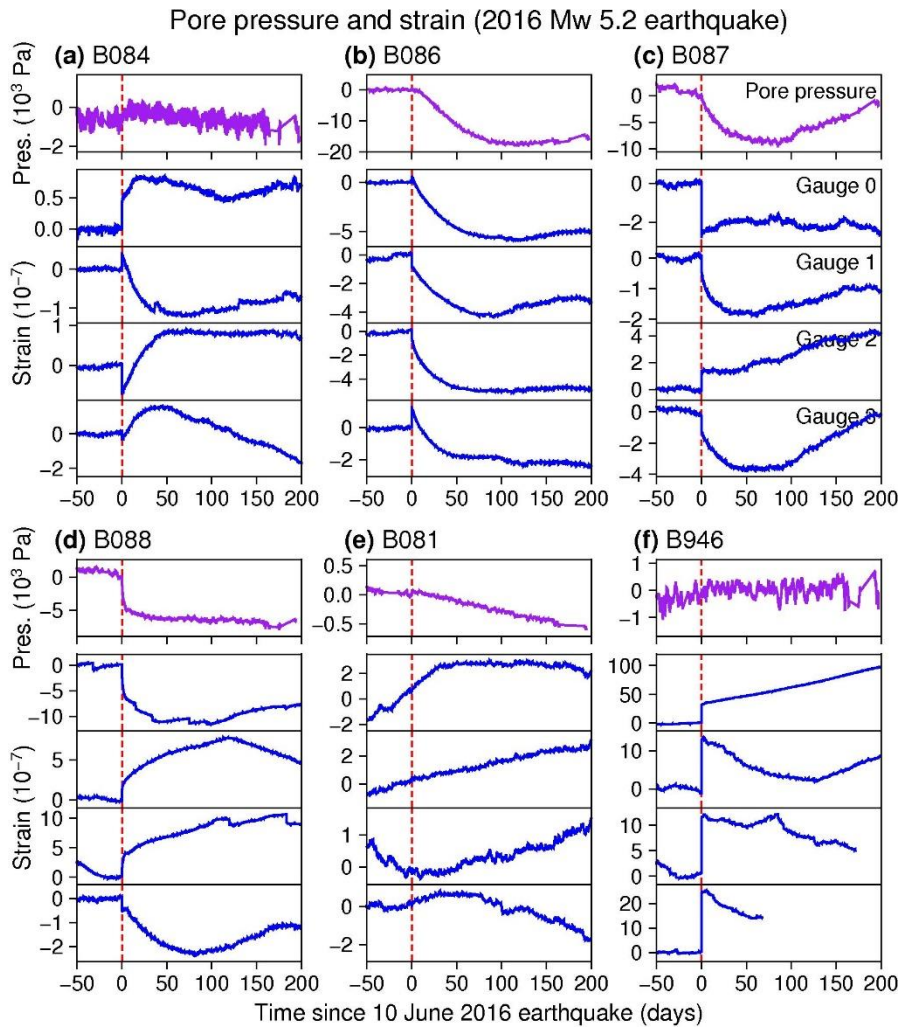
506 with vertical dashed lines (with magnitudes labeled beside). The shaded yellow bar

507 highlights the 2016 Mw 5.2 earthquake shown in Figure 2. Note the significant changes

508 of pore pressure and strain after each Mw 4.5+ earthquake.

509

510



511

512 **Figure 2. Pore pressure (purple curves) and strain (blue curves) before and after**

513 **the 2016 Mw 5.2 earthquake observed at strainmeters B084, B086, B087, B088,**

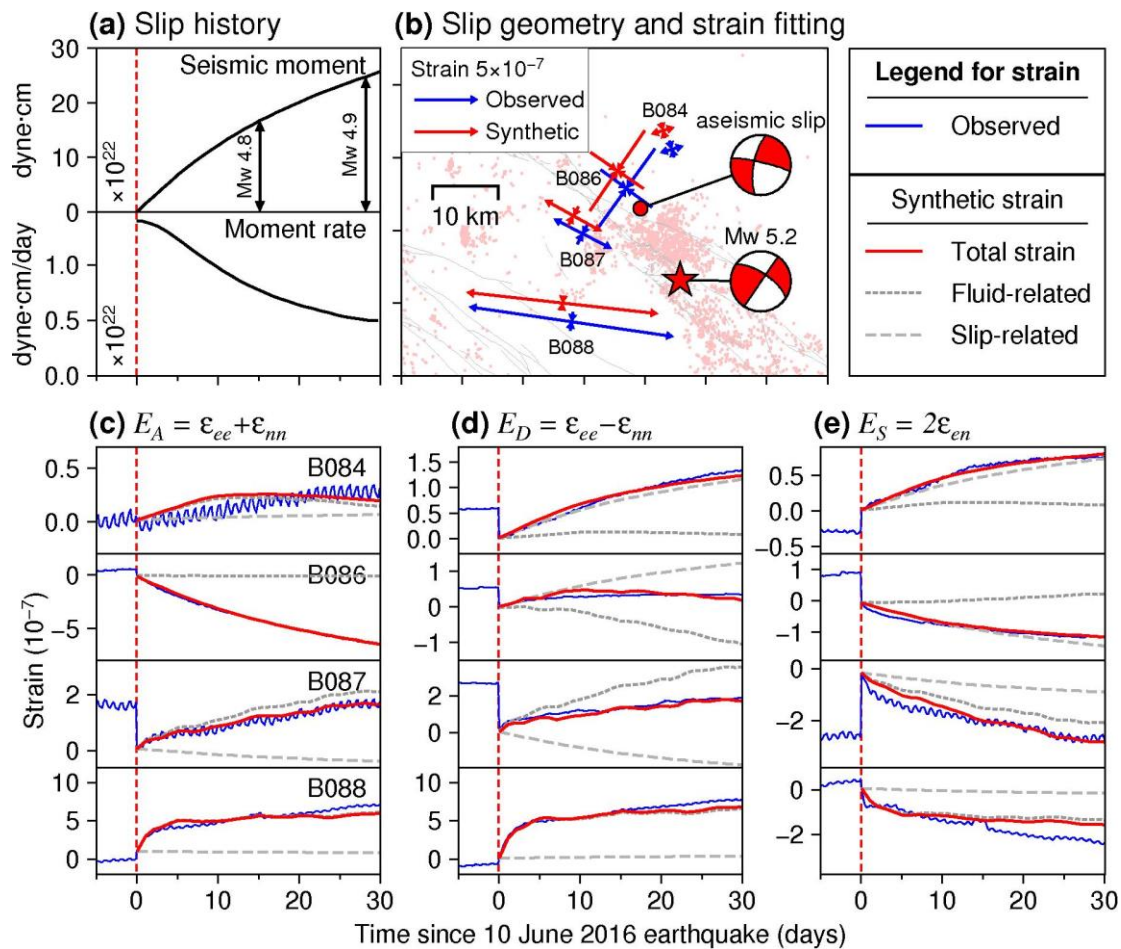
514 **B081 and B946.** Each strain component has been removed a linear trend before the

515 earthquake. The vertical dashed line in each panel marks the occurrence time of the

516 earthquake. Data containing large noise has been removed from gauges 2 and 3 of B946.

517

518



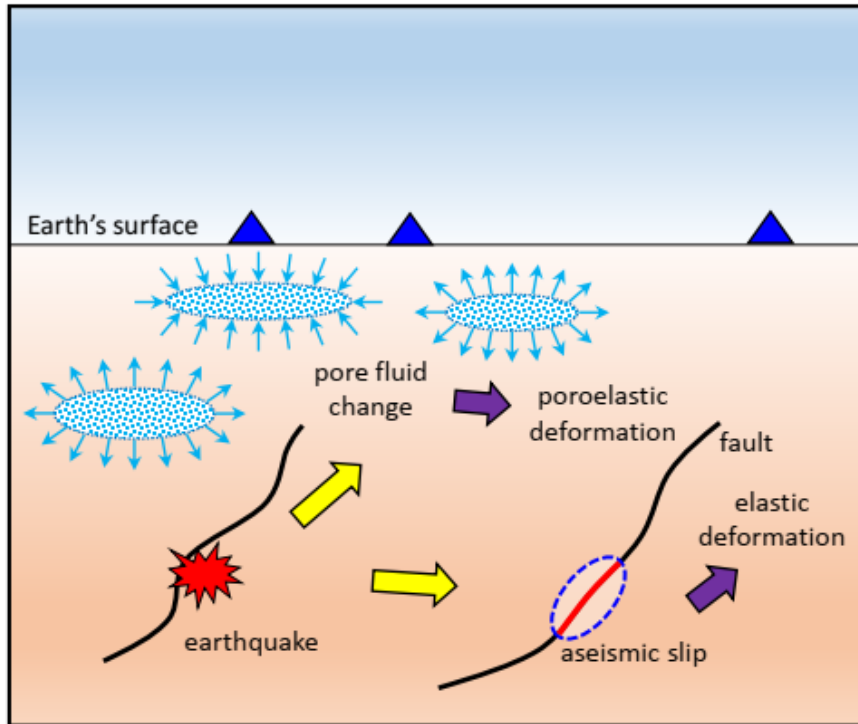
519

520 **Figure 3. The best-fitting postseismic aseismic slip and comparison between the**  
 521 **observed and synthetic postseismic strains. (a)** Seismic moment and moment rate of  
 522 the best-fitting aseismic slip as a function of time. **(b)** Location and focal mechanism  
 523 of the best-fitting aseismic slip, and a comparison between the observed and synthetic  
 524 postseismic strains (blue and red crosses, respectively) accumulated in the early 20 days  
 525 after the 2016 earthquake. The direction and length of the crosses represent orientation  
 526 and magnitude of the principal strains, with the vectors pointing outward (inward)  
 527 representing elongation (compression) in that orientation. Locations of the synthetic  
 528 strains are plotted offset for clarity. **(c–e)** Time series of the observed (blue solid curves)  
 529 and synthetic strains (red solid, grey short-dashed and grey long-dashed curves for the  
 530 total, fluid-related and slip-related strains, respectively) for (c) areal strain  $E_A$ , (d)

531 differential extension  $E_D$ , and (e) engineering shear strain  $E_S$ .

532

533



534

535 **Figure 4. Cartoon illustrating the physical mechanism in which an earthquake**

536 **triggers both pore fluid change and an aseismic slip, which subsequently produce**

537 **postseismic deformation.** The mainshock earthquake instantly triggers an aseismic

538 slip in a neighboring fault and alters the hydrological conditions in the region; the

539 change of hydrological condition results in postseismic pore pressure changes and

540 produces poroelastic deformation in the region, while the aseismic slip produces elastic

541 deformation.

542

1

2

*Geophysical Research Letters*

3

Supporting Information for

4

**Months-long crustal deformation driven by aseismic slips**

5

**and pore pressure transients triggered by local and regional**

6

**earthquakes**

7

8

9

**Zhou Lu<sup>1\*</sup>, Lianxing Wen<sup>2</sup>**

10

11 <sup>1</sup>Laboratory of Seismology and Physics of Earth's Interior; School of Earth and

12 Space Sciences, University of Science and Technology of China, Hefei, China

13 <sup>2</sup>Department of Geosciences, State University of New York at Stony Brook, Stony

14 Brook, NY, USA

15

16 \*Corresponding author: Zhou Lu ([luzhou@mail.ustc.edu.cn](mailto:luzhou@mail.ustc.edu.cn))

17

18

19 **Contents of this file**

20           Figures S1 to S6

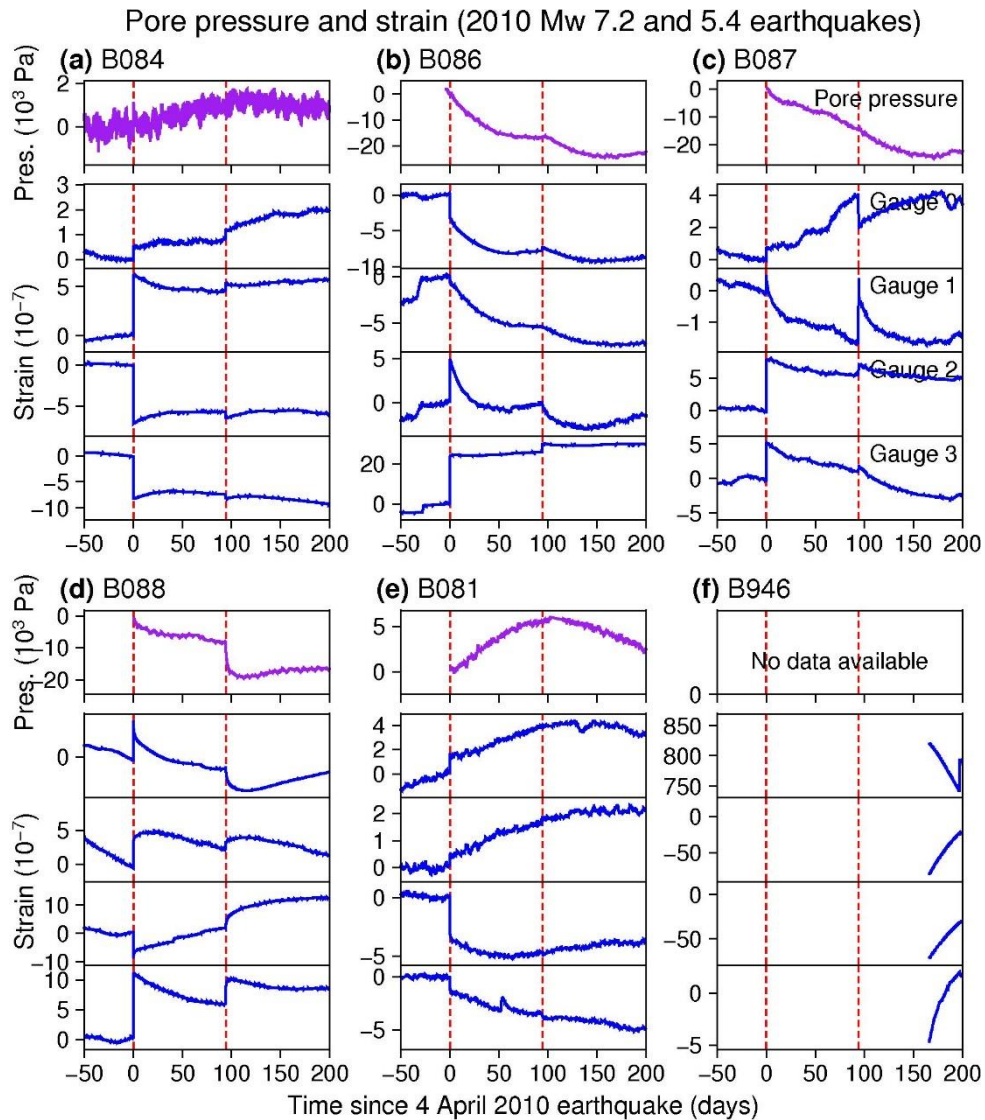
21

22 **Introduction**

23 This supporting information (SI) provides 6 figures, including: **(1)** Pore pressure and  
24 strain before and after the 4 April 2010 El Mayor-Cucapah and 7 July 2010 Collins  
25 Valley earthquakes (Figure S1), the 11 March 2013 Borrego range earthquake (Figure  
26 S2), and the 10 June 2016 Borrego Springs earthquake (Figure S3), **(2)** cumulative static  
27 strains at strainmeters produced by the aftershocks of the 10 June 2016 earthquake  
28 (Figure S4), **(3)** L-curve analysis for the strain fitting (Figure S5), and **(4)** comparison  
29 between the postseismic strains observed at the strainmeters used for qualitative  
30 constraint and those produced by the best-fitting aseismic slip (Figure S6).

31

32

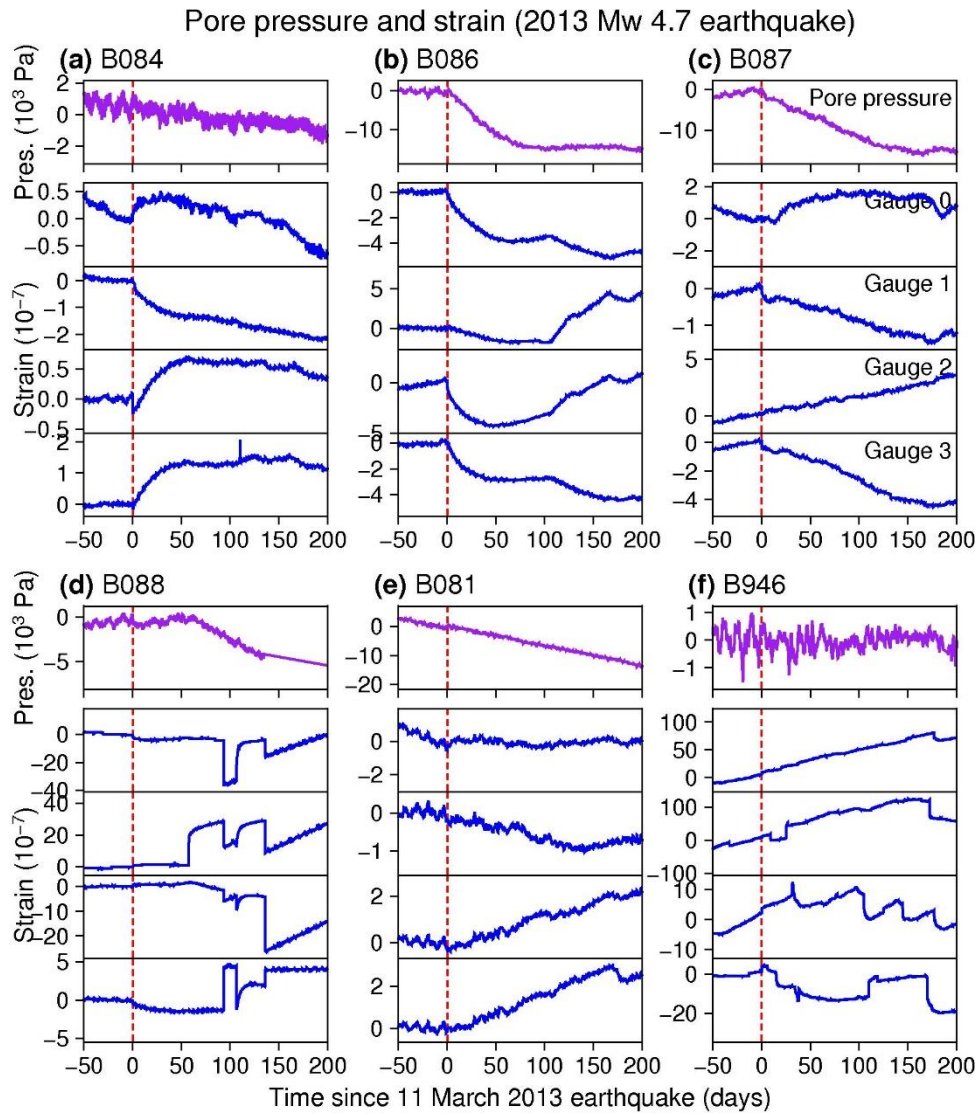


34

35 **Figure S1. Pore pressure (purple curves) and strain (blue curves) before and after**  
 36 **the 4 April 2010 El Mayor-Cucapah (Mw 7.2) and 7 July 2010 Collins Valley (Mw**  
 37 **5.4) earthquakes observed at strainmeters B084, B086, B087, B088, B081 and B946.**

38 The vertical dashed lines in each panel mark the occurrence times of the two  
 39 earthquakes.

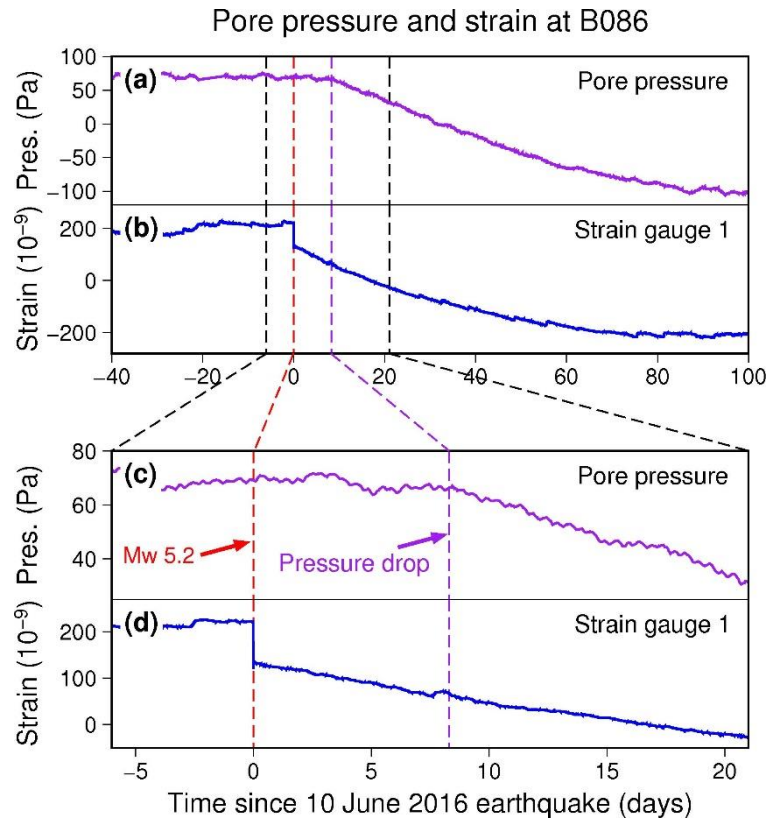
40



41

42 **Figure S2. Same as Figure S1, except for the 11 March 2013 Borrego range (Mw**  
 43 **4.7) earthquake.**

44



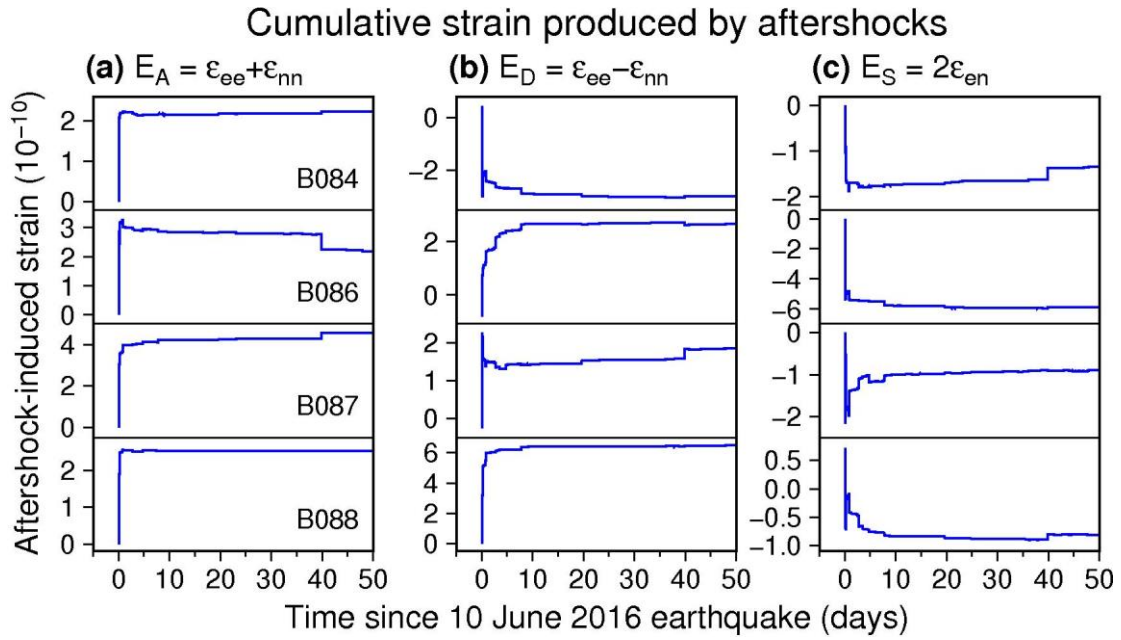
45

46 **Figure S3. Pore pressure and strain (gauge 1) observed at B086 before and after**  
 47 **the 10 June 2016 Mw 5.2 earthquake.** Note that the strain changes immediately after  
 48 the earthquake (red dashed line), while the pore pressure remains at background level  
 49 for about 8 days after the earthquake before exhibiting a significant decrease (purple  
 50 dashed line).

51

52

53

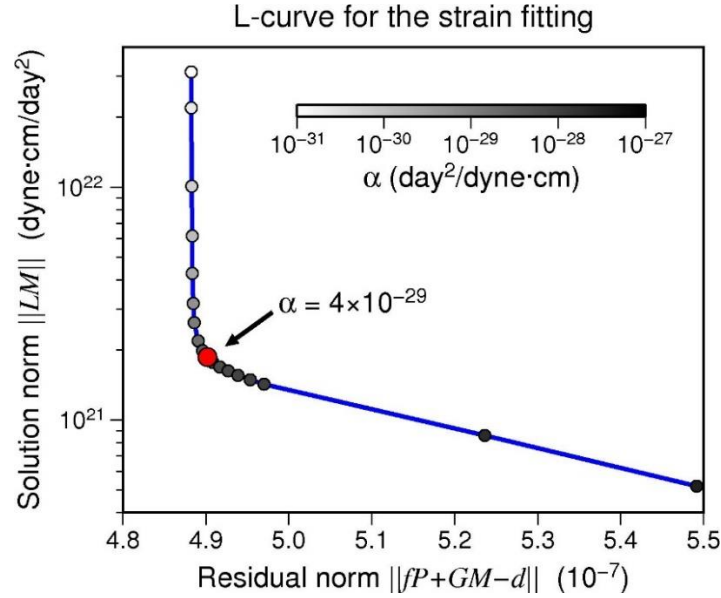


54

55 **Figure S4. Cumulative static strains at four strainmeters produced by the**  
 56 **aftershocks of the 10 June 2016 Mw 5.2 earthquake.** The strains are calculated using  
 57 Okada's method (Okada, 1985) in an elastic half-space Earth model, with the elastic  
 58 moduli being  $\lambda = 37.2$  GPa and  $\mu = 36.8$  GPa (Laske et al., 2013). The  
 59 hypocenters and focal mechanisms of the aftershocks are from the Southern California  
 60 Earthquake Data Center (<https://service.scedc.caltech.edu/eq-catalogs/FMsearch.php>),  
 61 with the focal mechanisms of the aftershocks with FMQ (focal mechanism quality) of  
 62 C, D or F replaced by that of the mainshock (strike/dip/rake =  $306^\circ/68^\circ/179^\circ$ ).

63

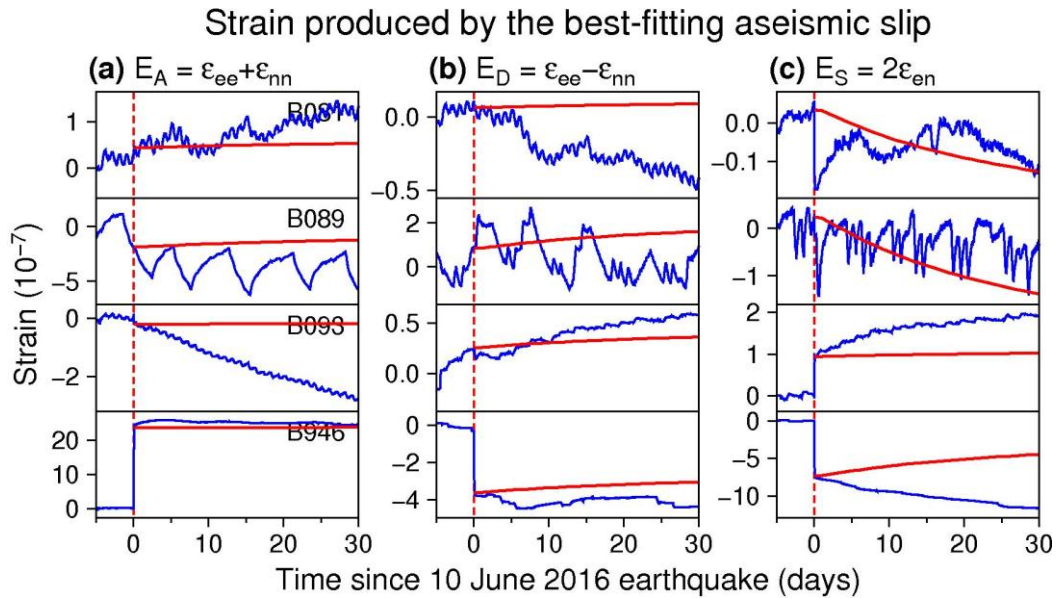
64



65

66 **Figure S5. L-curve analysis for the strain fitting based on Equation (2).** The corner  
 67 at  $\alpha = 4 \times 10^{-29}$  day<sup>2</sup>/dyne · cm is used as the smoothing parameter in the strain  
 68 fitting.

69



70

71 **Figure S6. Comparison between the postseismic strains observed at the**  
 72 **strainmeters used for qualitative constraint based on Equation (1) (blue) and those**  
 73 **produced by the best-fitting aseismic slip (red).**

74 **References**

75 Laske, G., Masters., G., Ma, Z., & Pasyanos, M. (2013). *Update on CRUST1.0 - A 1-*

76 *degree global model of Earth's crust*. Paper presented at the EGU.

77 Okada, Y. (1985). Surface deformation due to shear and tensile faults in a half-space.

78 *Bulletin of the Seismological Society of America*, 75(4), 1135–1154.

79